Rock and Soil Mechanics 2024 45(4): 1003−1013
https: //doi.org/10.26599/RSM.2024.9435583
ISSN 1000−7598
journal homepage: rocksoilmech.whrsm.ac.cn

A new calculation method for the size of anchor plates in unsaturated slope

PENG Jun-guo, HUANG Yu-hao
(School of Civil Engineering, Lanzhou University of Technology, Lanzhou, Gansu 730050, China)

Abstract: Due to its safety, stability, low cost and easy installation, anchor plate support structure has been widely used in the slope that needs to be reinforced. However, currently in the design process of anchor plate support structure, there is no mature calculation method for the size of anchor plate, resulting in overly conservative design. To address this issue, we propose using the limit equilibrium method in combination with log-spiral slip surface to calculate the active earth pressure in unsaturated soils. Based on the internal balance of the soil, the tensile force required to bear for each layer of anchor plate is calculated, and the calculation method for the size of the anchor plate is obtained. The minimum design length of the free section of the anchor plate is obtained according to the shape of the sliding surface. The calculation results of active earth pressure are compared with the existing literature, and it is found that the change trend of active earth pressure coefficient is consistent with the existing conclusions. The impacts of rainfall and earthquake conditions on the size of anchor plate are analyzed, and the results show that low rainfall intensity has a negligible effect on the size of anchor plate. However, when considering both strong rainfall and earthquake, the required anchor plate size can be significantly increased, with a maximum of 136.71%. The analysis results can provide reference for determining the size of frame anchor plates.
Keywords: anchor plate; unsaturated soil; active earth pressure; rainfall; earthquake

1 Introduction

The anchor plate support structure can provide great pull-out capacity to ensure the overall stability of the high filling slopes. Different from the conventional anchor slab structure, which is easily inclined in the construction process due to the vertical layout of the anchor slab, the anchor plate support structure can be installed directly on the surface of the backfill, thus eliminating the process of drilling and grouting. This has made it a popular choice in the construction of mountainous areas with complicated geological conditions. Zhuang et al.[1] carried out a series of model tests on the inclined shallow anchor plates in sand, and proposed a simple empirical method to predict their pull-out capacity. Shahriar et al.[2] proposed an analytical model for estimating the ultimate pull-out capacity of vertical anchor plates in frictional soil, which is capable of capturing more realistic changes in the pull-out capacity of anchor plates. Hanna et al.[3] established a numerical model using finite element technique and Mohr-Coulomb failure criterion to simulate the scenario of partially supporting retaining walls with embedded anchor plates in sandy soil, and provided a calculation method for the passive earth pressure on the embedded anchor plates. Bhattacharya et al.[4] used the lower bound theorem of limit analysis, in conjunction with finite element and linear optimization methods, to develop a method for determining the pull-out capacity of inclined anchor plates embedded in sandy soil. Kame et al.[5] proposed a numerical method for estimating the pull-out capacity of shallowly buried vertical anchor plates in cohesionless soil based on the Kotter equation. Zhu et al.[6] proposed a calculation formula for the pull-out capacity of anchor plates and a slope stability calculation method based on the limit equilibrium theory.

Peng et al.[7] calculated the active and passive earth pressures of unsaturated soil under transient seepage based on the variational analysis, and conducted numerical analysis on the parameters that affect the earth pressure. Based on the upper limit theorem of limit analysis, Li et al.[8] utilized the pseudo-dynamic method to analyze the three-dimensional stability of heterogeneous soil slope under seismic effect, and derived the explicit expression of the slope safety factor through the gravity increase method. Considering that the significant damage caused by vertical seismic action on slopes cannot be ignored, Tang et al.[9] proposed that in high-intensity mountainous areas, the seismic stability analysis of slopes should not only use the quasi-static method, but also adopt a more reasonable dynamic analysis method based on the time history for comprehensive analysis and evaluation. Zhang et al.[10] calculated the seismic effect of the sliding soil behind the wall by using the pseudo-dynamic method, and established the seismic active earth pressure solution of the inclined retaining wall under the change of water level by using the unsaturated soil mechanics principle and the limit equilibrium method. Ming et al.[11] applied the lower and upper limit methods of plasticity to establish a rigorous analytical solution for the ultimate lateral earth pressure of vertical plates of undrained cohesive soil. Shahrokhabadi et al.[12] calculated the static earth pressure, active earth pressure, and passive

Received: 11 May 2023 Accepted: 4 September 2023
First author: PENG Jun-guo, male, born in 1981, PhD, Associate Professor, research interests: unsaturated earth pressure. E-mail: pengjg@lut.edu.cn

earth pressure of unsaturated soil under transient flow, through Rankine earth pressure theory and the assumption of planar slip surface. Han et al.[13] used the VG function and Gardner function to describe the soil water characteristic curve and permeability coefficient curve, respectively, and obtained analytical solutions for rainfall infiltration using the traveling wave approximation and series expansion method. Zhu[14] applied log-spiral sliding surface to calculate the unsaturated active earth pressure of soil nail walls, and obtained the size calculation method for each layer of soil nails using the internal equilibrium of the slope.

At present, during the design process of the anchor plate support structure, the size of anchor plates is initially determined based on experience, and then verified by calculating the safety factor of slope[6]. There is no mature calculation method for determining the size of anchor plates, which leads to a conservative design. Based on the limit equilibrium method and the log-spiral slip surface, the active earth pressure of the anchor plate supporting structure of unsaturated slope is calculated. The ultimate pull-out capacity of each layer of anchor plate is obtained by the internal equilibrium of slope, and the calculation formula of the anchor plate size is derived. In the calculation process of this paper, rainfall, earthquake and other common conditions are considered, and the transient seepage is used to simulate rainfall. The seepage is a function of time, which is closer to the reality. The calculation method of anchor plate size derived in this paper can serve as a valuable reference for the design of anchor plate support structure.

2 Active earth pressure

2.1 Effective stress and shear strength of unsaturated soils

Lu et al.[15−16] defined the effective stress as follows:

$$\sigma' = \sigma - u_{\mathrm{a}} - \sigma^{\mathrm{s}} \tag{1}$$

where σ' represents the effective stress and σ represents the total stress; u_{a} denotes the pore air pressure, and by convention it is set to $u_{\mathrm{a}} = 0$; and σ^{s} is the suction defined by Lu et al.[15−16] as

$$\sigma^{\mathrm{s}} = -S_{\mathrm{e}}(u_{\mathrm{a}} - u_{\mathrm{w}}) \tag{2}$$

where u_{w} represents the pore water pressure; $u_{\mathrm{a}} - u_{\mathrm{w}}$ denotes the matric suction; S_{e} is the effective degree of saturation, which can be expressed as follows:

$$S_{\mathrm{e}} = \mathrm{e}^{-\alpha(u_{\mathrm{a}} - u_{\mathrm{w}})} \tag{3}$$

where α is a fitting parameter defined by the soil-water retention curve (kPa^{-1}).

Gardner's permeability coefficient function[17] is written by

$$k = k_{\mathrm{s}}\mathrm{e}^{-\alpha(u_{\mathrm{a}} - u_{\mathrm{w}})} \tag{4}$$

where k is the unsaturated permeability coefficient; and k_{s} is the saturated permeability coefficient.

Srivastava et al.[18] solved the Richards equation by using Eq. (4), and derived a solution for the normalized permeability coefficient K:

$$K = Q_{\mathrm{B}} - (Q_{\mathrm{B}} - \mathrm{e}^{-\mu h_0})\mathrm{e}^{-Y} - 4(Q_{\mathrm{B}} - Q_{\mathrm{A}})\mathrm{e}^{(L-Y)/2}\mathrm{e}^{-T/4} \times \sum_{n=1}^{\infty} \frac{\sin(\lambda_n Y)\sin(\lambda_n L)\mathrm{e}^{-\lambda_n T}}{1 + L/2 + 2\lambda_n^2 L} \tag{5}$$

where λ_n is the nth root of $\tan(\lambda L) + 2\lambda = 0$; h_0 is the initial suction head; and Y, L, K, Q_{A}, Q_{B} and T are dimensionless parameters calculated by following equation:

$$\left.\begin{aligned} & Y = \mu y; L = \mu H_1; K = \frac{k}{k_{\mathrm{s}}}; \\ & Q_{\mathrm{A}} = \frac{q_{\mathrm{A}}}{k_{\mathrm{s}}}; Q_{\mathrm{B}} = \frac{q_{\mathrm{B}}}{k_{\mathrm{s}}}; T = \frac{\mu k_{\mathrm{s}} t}{\theta_{\mathrm{s}} - \theta_{\mathrm{r}}} \end{aligned}\right\} \tag{6}$$

where y is the vertical coordinate representing the distance from the water table; H_1 is the depth from the ground surface to the water table; q_{A} is the initial steady flow into the ground surface at the time equal to zero; q_{B} is the flow into the ground surface at the time greater than zero; θ_{s} is the saturated volumetric water content and θ_{r} is the residual volumetric water content; $\mu = \alpha\gamma_{\mathrm{w}}$ is a parameter representing the decrease rate of permeability coefficient with increasing suction; and γ_{w} is the unit weight of water.

Substituting the initial conditions ($q_{\mathrm{A}} = 0$, $h_0 = 0$) into Eq. (5) yields the simplified expression:

$$K = Q_{\mathrm{B}} - (Q_{\mathrm{B}} - 1)\mathrm{e}^{-Y} - 4Q_{\mathrm{B}}\mathrm{e}^{(L-Y)/2}\mathrm{e}^{-T/4} \times \sum_{n=1}^{\infty} \frac{\sin(\lambda_n Y)\sin(\lambda_n L)\mathrm{e}^{-\lambda_n T}}{1 + L/2 + 2\lambda_n^2 L} \tag{7}$$

By combining Eqs. (2)−(4), (6) and (7), the suction can be expressed as a function of time and depth:

$$\sigma^{\mathrm{s}} = \frac{K}{\alpha}\ln K \tag{8}$$

Using the Mohr-Coulomb criterion, the shear strength is expressed as follows:

$$\tau = c' + \sigma'\psi \tag{9}$$

$$\psi = \tan\varphi' \tag{10}$$

where τ represents the shear strength at failure; and c' and φ' are the effective cohesion and friction angle, respectively.

2.2 Calculation model

In Fig. 1, H represents the height of the retaining wall; w is the angle between the wall face and the vertical axis; $y(x)$ is the slip surface function; $\bar{y}(x)$ is the slope surface function; the top of the slope is horizontal and subjected to the uniform surcharge Q; θ_0 and θ_1 are the angles of points 0 and 1, respectively; r is the radius of the log-spiral slip surface corresponding to the angle θ; τ is the shear strength along the slip surface;

σ is the normal stress distribution on $y(x)$; P_a is the resultant active earth pressure; D is the vertical distance from the action point of resultant force to the ground surface; q_B is the intensity of rainfall; k_h is the horizontal seismic coefficient; W is the weight of the soil mass within the unit width of the slip surface; B is the effective length of the uniform surcharge acting on the crest of the slope; k_hW and k_hQB are the horizontal inertial forces; and $(1\pm k_v)W$ and $(1\pm k_v)QB$ are the vertical inertial forces. The direction and sign of the vertical seismic coefficient k_v are defined as $[\downarrow +,\uparrow -]$. The water table is located at the bottom of the retaining wall.

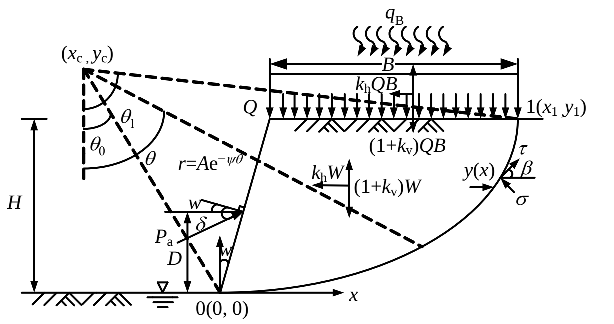

Fig. 1 Symbolic definition for calculating active earth pressure

By using the variational method similar to the approach taken by Baker et al.[19], the equilibrium equation of vertical force can be written as follows:

$$\int_l (\tau\sin\beta+\sigma\cos\beta)\,\mathrm{d}l+P_a\sin(\delta-w)-\int_0^{x_1}\gamma(1\pm k_v)(\bar{y}-y)\,\mathrm{d}x-\int_0^{x_1}Q(1\pm k_v)\mathrm{d}x+Q(1\pm k_v)H\tan w=0 \tag{11}$$

where γ is the unit weight of soil.

The equilibrium equation of horizontal force can be written as follows:

$$\int_l (\tau\cos\beta-\sigma\sin\beta)\,\mathrm{d}l+P_a\cos(\delta-w)-\int_0^{x_1}k_h\gamma(\bar{y}-y)\,\mathrm{d}x-\int_0^{x_1}Qk_h\mathrm{d}x+Qk_hH\tan w=0 \tag{12}$$

The moment equilibrium equation around the origin of the Cartesian coordinate system can be written as follows:

$$\int_l [y(\tau\cos\beta-\sigma\sin\beta)-x(\tau\sin\beta+\sigma\cos\beta)]\mathrm{d}l+P_a\cos(\delta-w)D-P_a\sin(\delta-w)D\tan w+\int_0^{x_1}[x\gamma(1\pm k_v)(\bar{y}-y)-k_h\gamma(\bar{y}-y)\frac{(\bar{y}+y)}{2}]\mathrm{d}x+\int_0^{x_1}Q(1\pm k_v)x\mathrm{d}x-Q(1\pm k_v)\frac{1}{2}(H\tan w)^2-\int_0^{x_1}Qk_hH\mathrm{d}x+Qk_hH^2\tan w=0 \tag{13}$$

where l is the arc length of the slip surface $y(x)$.

The geometric relations in Fig. 1 can be deduced as follows:

$$\left.\begin{aligned}\cos\beta&=\frac{\mathrm{d}x}{\mathrm{d}l}\\ \sin\beta&=\dot{y}\frac{\mathrm{d}x}{\mathrm{d}l}\end{aligned}\right\} \tag{14}$$

Substituting Eqs. (1), (9) and (14) into Eqs. (11)−(13), the equilibrium equation of vertical force can be written as follows:

$$\int_0^{x_1}[\dot{y}(c'+\sigma'\psi)+(\sigma'+\sigma^s)]\mathrm{d}x+P_a\sin(\delta-w)-\int_0^{x_1}\gamma(1\pm k_v)(\bar{y}-y)\,\mathrm{d}x-\int_0^{x_1}Q(1\pm k_v)\mathrm{d}x+Q(1\pm k_v)H\tan w=0 \tag{15}$$

The equilibrium equation of horizontal force can be expressed as follows:

$$\int_0^{x_1}[(c'+\sigma'\psi)-\dot{y}(\sigma'+\sigma^s)]\mathrm{d}x+P_a\cos(\delta-w)-\int_0^{x_1}k_h\gamma(\bar{y}-y)\,\mathrm{d}x-\int_0^{x_1}Qk_h\mathrm{d}x+Qk_hH\tan w=0 \tag{16}$$

The moment equilibrium equation around the origin of the Cartesian coordinate system can be rewritten as follows:

$$\int_0^{x_1}\{y[(c'+\sigma'\psi)-\dot{y}(\sigma'+\sigma^s)]-x[\dot{y}(c'+\sigma'\psi)+(\sigma'+\sigma^s)]+x\gamma(1\pm k_v)(\bar{y}-y)-k_h\gamma(\bar{y}-y)\frac{(\bar{y}+y)}{2}\}\mathrm{d}x+P_a\cos(\delta-w)D-P_a\sin(\delta-w)D\tan w+\int_0^{x_1}Q(1\pm k_v)x\mathrm{d}x-Q(1\pm k_v)\frac{1}{2}(H\tan w)^2-\int_0^{x_1}Qk_hH\mathrm{d}x+Qk_hH^2\tan w=0 \tag{17}$$

2.3 Equation of active earth pressure

Baker et al.[19] showed that combining Eqs. (15), (16) and (17) is equivalent to the minimization of an auxiliary function G:

$$\left.\begin{aligned}G&=\int_0^{x_1}g\mathrm{d}x\\ g&=L_0+\lambda_1L_1+\lambda_2L_2\end{aligned}\right\} \tag{18}$$

$$\left.\begin{aligned}L_0&=(\psi-\dot{y})\sigma'+c'-\dot{y}\sigma^s-k_h\gamma(\bar{y}-y)-Qk_h\\ L_1&=\sigma'(\dot{y}\psi+1)+\dot{y}c'+\sigma^s-(1\pm k_v)\gamma(\bar{y}-y)-\\ &\quad Q(1\pm k_v)\\ L_2&=\sigma'(y\psi-y\dot{y}-x\dot{y}\psi-x)+c'(y-x\dot{y})-\\ &\quad \sigma^s(y\dot{y}+x)+Q(1\pm k_v)x-Qk_hH\end{aligned}\right\} \tag{19}$$

where λ_1 and λ_2 are the Lagrange's undetermined multipliers.

Minimizing the function G can be achieved by considering the Euler differential equations for the function g:

$$\left.\begin{aligned}\frac{\partial g}{\partial \sigma'} &= \frac{\mathrm{d}}{\mathrm{d}x}\frac{\partial g}{\partial \dot{\sigma}'}\\ \frac{\partial g}{\partial y} &= \frac{\mathrm{d}}{\mathrm{d}x}\frac{\partial g}{\partial \dot{y}}\end{aligned}\right\} \tag{20}$$

As demonstrated by Eqs. (18) and (19), the function g is independent of $\dot{\sigma}'$. Consequently, the first equation in Eq. (20) can be simplified as follows:

$$\frac{\partial g}{\partial \sigma'} = 0 \tag{21}$$

Combining Eqs. (18), (19) and (21) yields

$$\psi[(-1-\lambda_2 y) + \dot{y}(-\lambda_1 + \lambda_2 x)] + \dot{y}(1+\lambda_2 y) - \lambda_1 + \lambda_2 x = 0 \tag{22}$$

or

$$\psi[(-\frac{1}{\lambda_2} - y) + \dot{y}(-\frac{\lambda_1}{\lambda_2} + x)] + \dot{y}(\frac{1}{\lambda_2} + y) - \frac{\lambda_1}{\lambda_2} + x = 0 \tag{23}$$

Eq. (23) can be solved as

$$\dot{y} = \frac{\mathrm{d}y}{\mathrm{d}x} = \frac{(\frac{\lambda_1}{\lambda_2} - x) + \psi(\frac{1}{\lambda_2} + y)}{\psi(-\frac{\lambda_1}{\lambda_2} + x) + (\frac{1}{\lambda_2} + y)} \tag{24}$$

where $\lambda_2 \neq 0$. If $\lambda_2 = 0$, the slip surface will degenerate into a plane, which is beyond the scope of this paper.

Eq. (24) can be simplified by using the following polar coordinate transformation:

$$\left.\begin{aligned} y + \frac{1}{\lambda_2} &= -r\cos\theta \\ x - \frac{\lambda_1}{\lambda_2} &= r\sin\theta \end{aligned}\right\} \tag{25}$$

By combining Eqs. (24) and (25), r can be expressed as follows:

$$r = A\mathrm{e}^{-\psi\theta} \tag{26}$$

Note that Eq. (26) represents a series of log-spirals with the pole $(x_c, y_c) = (\frac{\lambda_1}{\lambda_2}, -\frac{1}{\lambda_2})$.

According the geometric relations in Fig. 1, substituting the coordinates of points 0 and 1 into Eq. (25) yields

$$A = \frac{H}{\mathrm{e}^{-\psi\theta_0}\cos\theta_0 - \mathrm{e}^{-\psi\theta_1}\cos\theta_1} \tag{27}$$

The minimization of an auxiliary function G is consistent with the moment equilibrium equation around the pole of the log-spiral[19], i.e.

$$\begin{aligned}&\int_0^{x_1}\{(y-y_\mathrm{c})[(c'+\sigma'\psi) - \dot{y}(\sigma'+\sigma^\mathrm{s})] - \\ &(x-x_\mathrm{c})[\dot{y}(c'+\sigma'\psi) + (\sigma'+\sigma^\mathrm{s})] + \\ &(x-x_\mathrm{c})\gamma(1\pm k_\mathrm{v})(\bar{y}-y) + k_\mathrm{h}\gamma(\bar{y}-y)(y_\mathrm{c} - \\ &\frac{(\bar{y}+y)}{2})\}\mathrm{d}x - P_\mathrm{a}\cos(\delta-w)(y_\mathrm{c}-D) - \\ &P_\mathrm{a}\sin(\delta-w)(D\tan w - x_\mathrm{c}) + \int_0^{x_1} Q(1\pm k_\mathrm{v})\cdot \\ &(x-x_\mathrm{c})\mathrm{d}x - Q(1\pm k_\mathrm{v})H\tan w(\frac{1}{2}H\tan w - x_\mathrm{c}) + \\ &\int_0^{x_1} Qk_\mathrm{h}(y_\mathrm{c}-H)\mathrm{d}x - Qk_\mathrm{h}H\tan w(y_\mathrm{c}-H) = 0\end{aligned} \tag{28}$$

Equation (28) can be simplified as follows:

$$\begin{aligned}&P_\mathrm{a}\cos(\delta-w)(r_0\cos\theta_0 - D) + \\ &P_\mathrm{a}\sin(\delta-w)(D\tan w + r_0\sin\theta_0) = \\ &\int_{\theta_0}^{\theta_1} r^2(\psi\sigma^\mathrm{s} - c')\mathrm{d}\theta + \int_{\theta_0}^{\theta_1}[r^2\sin\theta\gamma(1\pm k_\mathrm{v})\cdot \\ &(r\cos\theta - r_1\cos\theta_1)(-\psi\sin\theta + \cos\theta)]\mathrm{d}\theta + \\ &\int_{\theta_0}^{\theta_1}[k_\mathrm{h}\gamma(r\cos\theta - r_1\cos\theta_1)(\frac{r\cos\theta + r_1\cos\theta_1}{2})\cdot \\ &(r\cos\theta - r\psi\sin\theta)]\mathrm{d}\theta - \\ &\frac{1}{2}\gamma(1\pm k_\mathrm{v})H^2\tan w(\frac{H}{3}\tan w + r_0\sin\theta_0) - \\ &\frac{1}{2}k_\mathrm{h}\gamma H^2\tan w(r_0\cos\theta_0 - \frac{2}{3}H) + \\ &[Q(1\pm k_\mathrm{v})(r_1\sin\theta_1 - r_0\sin\theta_0 - H\tan w)\cdot \\ &\frac{1}{2}(r_0\sin\theta_0 + H\tan w + r_1\sin\theta_1) + k_\mathrm{h}Q\cdot \\ &(r_1\sin\theta_1 - r_0\sin\theta_0 - H\tan w)(r_0\cos\theta_0 - H)]\end{aligned} \tag{29}$$

Following the classic active earth pressure expressions, Eq. (29) can be rewritten as

$$P_\mathrm{a} = \frac{1}{2}K_\mathrm{a}\gamma H^2 \tag{30}$$

where K_a is the coefficient of active earth pressure.

The second Euler equation in Eq. (20) solves the distribution function of σ'. Because the σ' distribution is not necessary to assess the resultant active earth pressure acting on a retaining wall, the second equation in Eq. (20) is omitted in this work.

Equation (29) considers the effect of the wall-soil friction angle δ on the resultant active earth pressure. Figure 2 depicts the changes of the coefficient of active earth pressure for fine sand with the wall-soil friction angle and seepage time, where H=4 m, $q_\mathrm{B} = 5.0\times10^{-6}$ m/s, $Q = 0$ kN/m, $c' = 0.0$ kPa, $q_\mathrm{A} = 0$ m/s, $w = 0^\circ$, $\gamma = 18$ kN/m^3, $\varphi' = 40^\circ$, $\alpha = 0.07$ kPa^{-1}. As shown in Fig. 2, the coefficient of active earth pressure increases with the seepage time. As the seepage time elapses, the backfill gradually saturates, leading to a stabilization of the earth pressure coefficient. Decreasing the wall-soil friction angle increases the coefficient of active earth pressure.

When the retaining wall face is a flexible structure such as the frame, it is difficult for the wall-soil friction angle to be fully utilized. In design, the effect of wall-soil friction angle should be ignored, and then a safer design could be achieved.

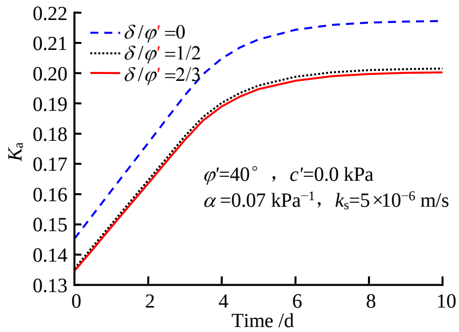

Fig. 2 Influence of different δ/φ' values on active earth pressure coefficient

Leshchinsky et al.[20] pointed out that for rigid wall faces such as masonry blocks, the direction of active earth pressure is horizontal and is independent of the wall-soil friction angle, similar to that of the flexible wall faces. By setting the direction of the earth pressure as horizontal, the resultant active earth pressure can be rewritten as follows:

$$
\begin{aligned}
P_a = \{ & \int_{\theta_0}^{\theta_1} r^2 (\psi\sigma^s - c')\,\mathrm{d}\theta + \\
& \int_{\theta_0}^{\theta_1} [r^2 \sin\theta\gamma(1 \pm k_v)(r\cos\theta - r_1\cos\theta_1) \cdot \\
& (-\psi\sin\theta + \cos\theta)]\mathrm{d}\theta + \\
& \int_{\theta_0}^{\theta_1} [k_h\gamma(r\cos\theta - r_1\cos\theta_1)(\frac{r\cos\theta + r_1\cos\theta_1}{2}) \cdot \\
& (r\cos\theta - r\psi\sin\theta)]\mathrm{d}\theta - \\
& \frac{1}{2}\gamma(1 \pm k_v)H^2 \tan w(\frac{H}{3}\tan w + r_0\sin\theta_0) - \\
& \frac{1}{2}k_h\gamma H^2 \tan w(r_0\cos\theta_0 - \frac{2}{3}H) + \\
& [Q(1 \pm k_v)(r_1\sin\theta_1 - r_0\sin\theta_0 - H\tan w) \cdot \\
& \frac{1}{2}(r_0\sin\theta_0 + H\tan w + r_1\sin\theta_1) + \\
& k_h Q(r_1\sin\theta_1 - r_0\sin\theta_0 - H\tan w) \cdot \\
& (r_0\cos\theta_0 - H)]\} / (r_0\cos\theta_0 - D)
\end{aligned} \tag{31}
$$

2.4 Comparison with other approaches

To verify the accuracy of the calculation results in this study, the results for silt and fine sand are compared with those obtained by Shahrokhabadi et al.[12]. The soil parameters are listed in Table 1[12,17].

In addition to the soil parameters listed in Table 1, other parameters are given as follows: $H = 4$ m, $w = 0^\circ$, $Q = 0$ kN/m , $Q_A = 0$, $Q_B = 1$, $\gamma = 18$ kN/m^3 , $\delta / \varphi' = 0$.

The comparison results of the active earth pressure coefficient for silt are shown in Fig. 3. The corresponding spatiotemporal variations of suction within the soil and the trajectory changes of the most critical slip surface are depicted in Figs. 4 and 5, respectively. From Fig. 3, it can be observed that the active earth pressure coefficient of silt increases rapidly within 0−150 d and stabilizes after 250 d. The main reason for this is that rainfall leads to a decrease in the internal suction of the soil. As shown in Fig. 4, the maximum suction occurs in the upper-middle part of the soil, and the suction near the water table approaches 0. As shown in Fig. 3, after approximately 360 d of rainfall infiltration, the soil reaches saturation and the suction completely disappears, resulting in no further change in active earth pressure. From the early stages of intense rainfall to the soil saturation, the active earth pressure coefficients of log-spiral slip surface and planar slip surface increase by 58.56% and 44.05%, respectively.

Table 1 Mechanical properties of soils

Soil type	α/ kPa^{-1}	k_s/ (m • s^{-1})	θ_s	θ_r	c'/ kPa	φ'/ (°)
Silt	0.05	1×10^{-7}	0.45	0.10	1.7	30
Fine sand	0.07	5×10^{-6}	0.41	0.05	0.0	40

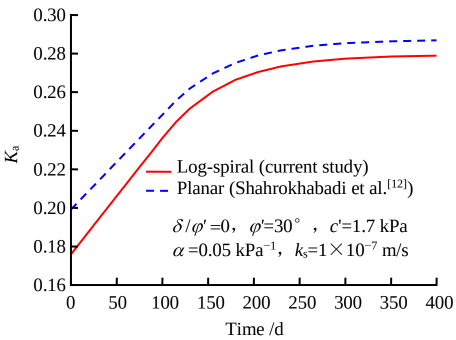

Fig. 3 Relationships between active earth pressure coefficient obtained by using plane and log-spiral slip surfaces and time (silt)

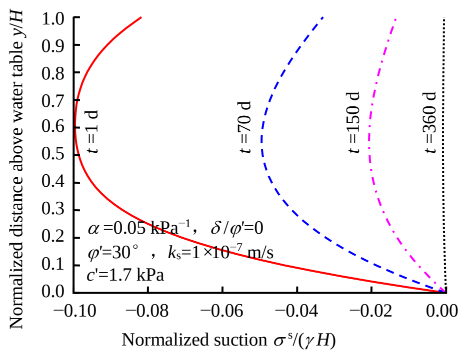

Fig. 4 Spatiotemporal distributions of suction in silt

Furthermore, Fig. 3 illustrates that the active earth pressure coefficient calculated based on the log-spiral slip surface is slightly lower than that obtained by Shahrokhabadi et al.[12] based on the planar slip surface.

The difference between the two approaches gradually diminishes over time with the progression of infiltration, eventually approaching stability. In the classic soil mechanics, without considering the effect of suction, the active earth pressure derived from the log-spiral slip surface is greater than that from the planar slip surface. When considering the effect of suction, a different trend is observed compared to the classic soil mechanics. This is due to the fact that the contribution of suction resisting sliding is greater for the log-spiral slip surface compared to the planar slip surface, resulting in a lower active earth pressure. The trend of comparison between active earth pressure using different sliding surfaces in this study is consistent with the conclusions in the literature[7]. As shown in Fig. 5, with the progression of rainfall infiltration, the pole of the most critical log-spiral slip surface gradually moves away from the slope surface, causing the curved surface within the soil to gradually approach the planar slip surface. The difference in the contribution of suction between the two slip surfaces gradually decreases over time. Therefore, the gap between the active earth pressure coefficients calculated based on the two slip surfaces gradually shrinks with the infiltration time until it becomes stable.

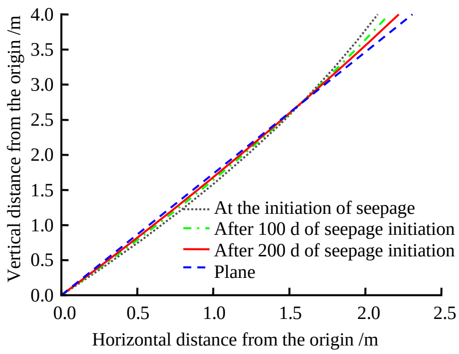

Fig. 5 Comparisons of plane and log-spiral slip surfaces (silt)

The comparison results of the active earth pressure for fine sand are shown in Fig. 6, and the corresponding spatiotemporal variations of suction within the soil are shown in Fig. 7. The variations in the active earth pressure coefficient of fine sand and the changes in suction are similar to silt. However, due to its larger permeability coefficient, fine sand reaches full saturation just after 10 d of rainfall. Soil with larger permeability coefficients can more quickly reach saturation, which means that suction will dissipate in a shorter time. As the suction within fine sand is lower than that in the silt, the difference in the active earth pressure coefficients calculated based on the log-spiral slip surface and the planar slip surface also decreases accordingly, as shown in Fig. 6. Furthermore, the two slip surfaces are closer to each other in fine sand compared to silt, as shown in Fig. 8.

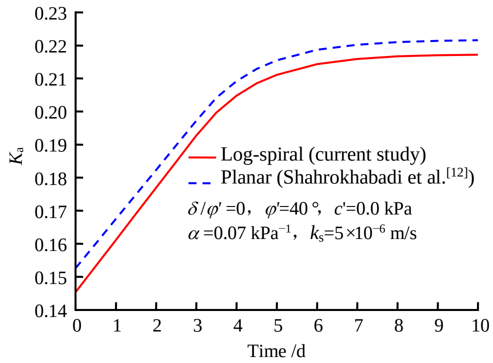

Fig. 6 Relationships of active earth pressure coefficient obtained by using plane and log-spiral slip surfaces with time (fine sand)

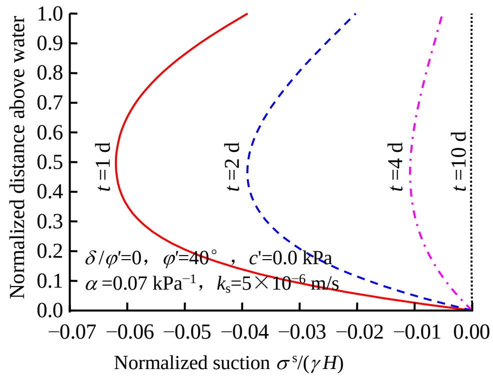

Fig. 7 Spatiotemporal distributions of suction in fine sand

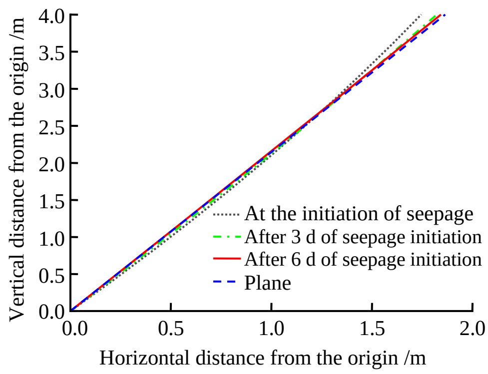

Fig. 8 Comparisons of plane and log-spiral slip surfaces (fine sand)

3 Calculation of the size of anchor plates

3.1 Distribution of force borne by anchor plate along depth

The arrangement of the anchor plate support structure on the slope is shown in Fig. 9. By using the method similar to Vahedifard et al.[21] for determining the size of soil nails, the sum of the horizontal tensile forces borne by each layer of anchor plates should be in equilibrium with the resultant active earth pressure, i.e.

$$P_a = T = \sum_{i=1}^{n} T_{\max-i} \tag{32}$$

where $T_{\max-i}$ represents the horizontal tensile force borne by the i-th layer of anchor plates; n is the number of layers of anchor plates; and T is the sum of the horizontal tensile forces borne by each layer of anchor plates. The P_a is calculated using Eq. (31), i.e. the active earth pressure is in the horizontal direction[20].

As shown in Fig. 10, due to the widespread application of frame anchor plate support structure at present, the influence of the frame wall face on the active earth pressure is minimal, and it can be neglected in the calculation, which will result in a safer design.

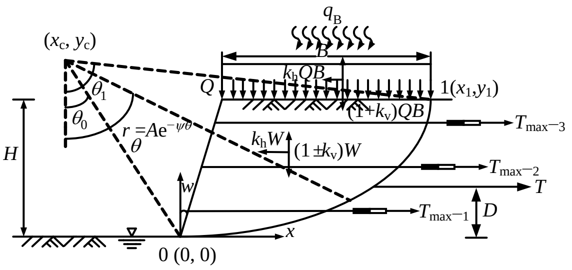

Fig. 9 Calculation diagram of tensile bearing capacity of anchor plate

Fig. 10 A slope supported by frame anchor plates

The resultant active earth pressure is distributed to each layer of anchor plates as follows:

(1) The sum of distribution coefficients for each layer of anchor plates is calculated by

$$\sum_{i=1}^{n} D_{T_{\max-i}} \tag{33}$$

where $D_{T_{\max-i}}$ represents the distribution coefficients for the i-th layer of anchor plates.

(2) The horizontal tensile force $T_{\max-i}$ borne by the i-th layer of anchor plates is calculated by

$$T_{\max-i} = P_a \frac{D_{T_{\max-i}}}{\sum_{i=1}^{n} D_{T_{\max-i}}} \tag{34}$$

In this study, both the linear distribution assumed by the theory and the trapezoidal distribution proposed by Allen et al.[22] based on the experimental results are considered for allocating the active earth pressure to each layer of anchor plates. With a wall height of 6 m and 3 layers of anchor plates installed, the distribution coefficients for the linear and trapezoidal distributions are shown in Figs. 11 and 12, respectively.

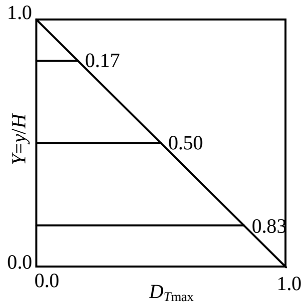

Fig. 11 Coefficients of each layer under linear distribution

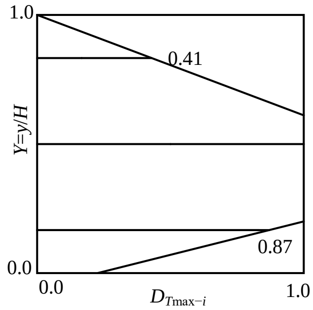

Fig. 12 Coefficients of each layer under trapezoidal distribution

3.2 Calculation equations for the size of anchor plates

The photo and force diagram of the anchor plate are shown in Fig. 13. Due to the relatively small side area of the anchor plate, the non-limit passive earth pressure on the side connected to the anchor plate and tie rod is neglected, resulting in a safer design. Zhu et al.[6] derived the formula for calculating the ultimate pull-out capacity of the anchor plates as follows:

$$T_p = 2F \tag{35}$$

where T_p is the ultimate pull-out capacity of the anchor plates; and F is the frictional resistance at the interface between the anchor plate and the soil:

$$F = \tau A_f \tag{36}$$

where τ is the shear strength of the interface between the anchor plate and the soil; and A_f is the contact area between the anchor plate and the soil, which is the area of the upper (lower) surface of the anchor plate.

$$\tau = f(\gamma h + \sum \Delta\sigma) + c' \tag{37}$$

where γh is the vertical self-weight of the soil; h is the height of the soil above the anchor plate; $\sum \Delta\sigma$ is vertical additional pressure caused by the uniform surcharge; and f is the friction coefficient between the anchor plate and the soil, which should be determined by the experiment.

The ultimate pull-out capacity of the i-th anchor plate should be greater than the horizontal tensile force $T_{\max-i}$ in order to satisfy the pull-out stability of the anchor plate, expressed as follows:

$$2[f(\gamma h + \sum \Delta\sigma) + c']A_f \geqslant P_a \frac{D_{T_{\max-i}}}{\sum_{i=1}^{n} D_{T_{\max-i}}} \tag{38}$$

(a) Photo

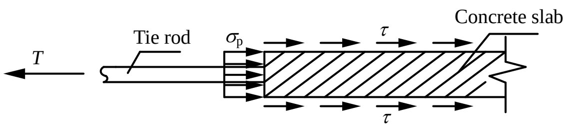

(b) Stress diagram

Fig. 13 Photo and stress diagram of anchor plate

The minimum anchorage size of the anchor plate can be obtained as follows:

$$A_f \geqslant [P_a \frac{D_{T\max-i}}{\sum_{i=1}^{n} D_{T\max-i}}]/2[f(\gamma h+\sum\Delta\sigma)+c'] \qquad (39)$$

4 Parametric analysis

In order to investigate the influences of rainfall and seismic conditions on the design of anchor plate size, the parametric analysis is conducted on rainfall intensity Q_B, horizontal seismic coefficient k_h and vertical seismic coefficient k_v. The active earth pressure is distributed to each layer of anchor plates with linear distribution and trapezoidal distribution proposed by Allen et al.[22], as shown in Figs. 11 and 12, respectively.

In this section, silt is selected, with relevant parameters as shown in Table 1. The height of the retaining wall is 6 m, and the first layer of anchor plate is located 1 m above the bottom of the retaining wall, with each subsequent layer installed every 2 m upwards. The angle between the wall face and the vertical axis is 10°, and the uniform surcharge acting on the top of the slope is 10 kN/m. The friction coefficient f between the anchor plate and the soil is 0.3[6]. The water table is located at the bottom of the retaining wall, and the unit weight of the soil is 18 kN/m^3.

4.1 Effect of rainfall intensity on design size of anchor plates

Figures 14 and 15 respectively illustrate the variation of design size of anchor plates under trapezoidal and linear distributions with rainfall intensity. The design size of each layer of anchor plates are different due to the difference of the action point of the resultant force and the tension borne by each layer of anchor plates under different distributions. Under the linear distribution, the height D of the action point of the resultant force is taken as $H/3$, and the calculated size of the anchor plate increases layer by layer from top to bottom. However, under the trapezoidal distribution proposed by Allen et al.[22], the height D of the resultant force is taken as $0.45H$, with the middle layer of anchor plate having the largest design size, followed by the top layer, and the design size of the bottom layer of anchor plate being the smallest. This is primarily because under the trapezoidal distribution, the distribution coefficient of the anchor plate at the bottom layer is relatively small. Moreover, due to the larger vertical self-weight of the soil at the bottom layer, the frictional resistance provided by the contact surface between the anchor and the soil also increases, which results in the smallest design size for the bottom layer of anchor plates.

In both trapezoidal and linear distributions, it can be observed that the influence of rainfall on the design size of anchor plates can be neglected (with increment less than 2%), when the rainfall intensity is low ($Q_B \leqslant 0.5$). As the rainfall intensity reaches a certain value, the design size of anchor plates increases significantly. Compared to the situation without rainfall ($Q_B = 0$), the design size of anchor plates under trapezoidal and linear distributions is increased by 29.94% and 30.31%, respectively, when considering heavy rainfall ($Q_B = 1$). This indicates the importance of considering the effect of heavy rainfall in the design of anchor plate size.

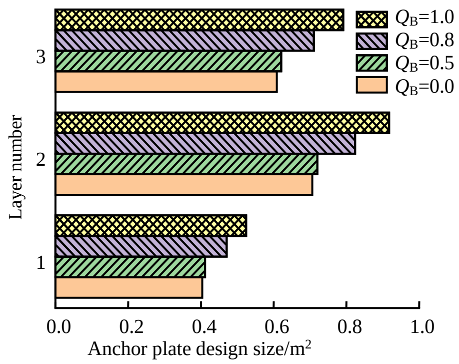

Fig. 14 Design sizes of anchor plates for each layer under different rainfall intensities with trapezoidal distribution

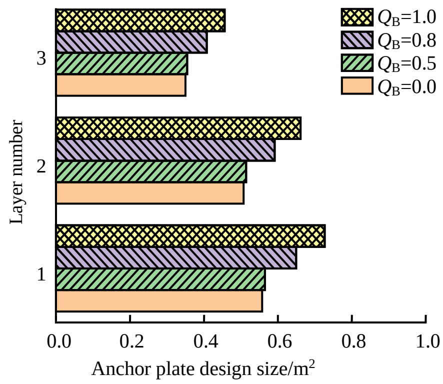

Fig. 15 Design sizes of anchor plates for each layer under different rainfall intensities with linear distribution

4.2 Effect of seismic action on design size of anchor plates

Figures 16 and 17 respectively depict the variations of the design size of anchor plates with the horizontal seismic coefficient and the vertical seismic coefficient (downward) under the trapezoidal and linear distributions. For ease of analysis, $k_{\rm h}/k_{\rm v}=1$ is taken, and $k_{\rm h}=0$ represents no seismic action. Figure 16 indicates that when using the trapezoidal distribution, compared to the case without considering seismic action, the design size of anchor plates increases by 44.80% and 95.58% when $k_{\rm h}$ is set to 0.1 and 0.2, respectively. Under the linear distribution, compared to the case without considering seismic action, the design size of anchor plates increases by 47.87% and 103.17% when $k_{\rm h}$ is set to 0.1 and 0.2, respectively.

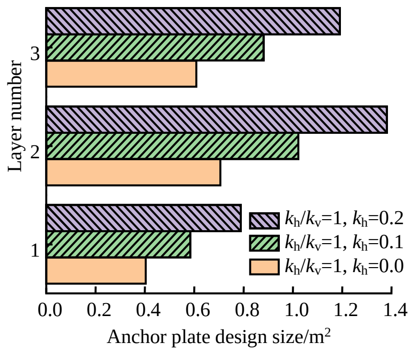

Fig. 16 Design sizes of anchor plates for each layer under different seismic intensities with trapezoidal distribution (vertical seismic coefficient downward)

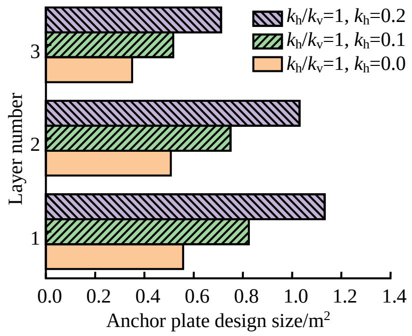

Fig. 17 Design sizes of anchor plates for each layer under different seismic intensities with linear distribution (vertical seismic coefficient downward)

Figures 18 and 19 respectively show the variations of design size of anchor plates with the horizontal seismic coefficient and the vertical seismic coefficient (upward) under the trapezoidal and linear distributions, where $k_{\rm h}/k_{\rm v}=-1$ is taken. Figure 18 shows that when using the trapezoidal distribution, compared to the case without considering seismic action, the design size of anchor plates increases by 15.47% and 42.16% when $k_{\rm h}$ is set to 0.1 and 0.2, respectively. Under the linear distribution, compared to the case without considering seismic action, the design size of anchor plates increases by 18.28% and 49.28% when $k_{\rm h}$ is set to 0.1 and 0.2, respectively.

Compared with the case without considering the seismic effect, the increase in design size of anchor plates under case $k_{\rm h}/k_{\rm v}=1$ is much greater than that under $k_{\rm h}/k_{\rm v}=-1$. This indicates that the vertical downward seismic force will increase the tension borne by each layer of anchor plates, and the design size of anchor plates increases. When designing frame anchor plate retaining walls, the most unfavorable conditions should be considered, thus the effects of horizontal and vertical downward seismic forces need to be taken into account.

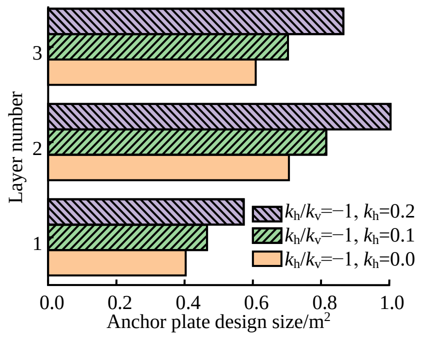

Fig. 18 Design sizes of anchor plates for each layer under different seismic intensities with trapezoidal distribution (vertical seismic coefficient upward)

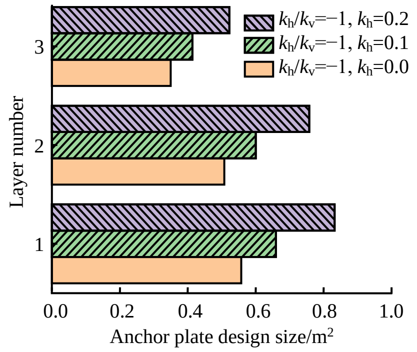

Fig. 19 Design sizes of anchor plates for each layer under different seismic intensities with linear distribution (vertical seismic coefficient upward)

4.3 Combined effects of heavy rainfall and seismic action on design size of anchor plates

Figure 20 shows the variations of design size of anchor plates under the trapezoidal distribution considering the effects of both rainfall and seismic activity. From Fig. 20, it can be observed that under the most unfavorable conditions, i.e. heavy rainfall ($Q_{\rm B}=1$) is considered and both horizontal and vertical seismic coefficients are taken as 0.2, the design size of anchor plates increases by 126.77% compared with the case without considering rainfall and seismic effects. Similarly, as depicted in Fig. 21, when considering the most unfavorable scenario under the linear distribution, the design size of anchor plates increases by 136.71% compared with the case without considering rainfall and seismic effects.

The aforementioned analysis indicates that heavy rainfall and seismic activity have a significant influence on the design size of anchor plates. During designing the size of anchor plates, heavy rainfall and seismic activity must be fully considered. By comparing the design size of anchor plates under the linear and trapezoidal distributions for various cases, it is observed that the sum of the size of each layer of anchor plates under linear distribution is 19.51%−22.15% smaller than that under trapezoidal distribution. Therefore, the anchor plate size designed according to trapezoidal distribution is safer.

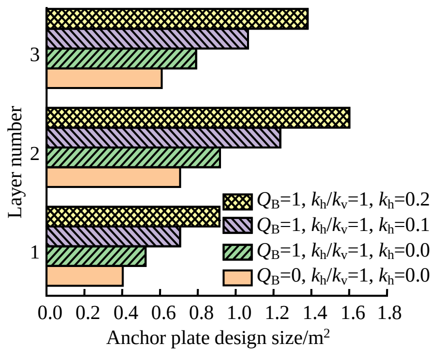

Fig. 20 Design sizes of anchor plates for each layer considering different seismic and rainfall intensities with trapezoidal distribution

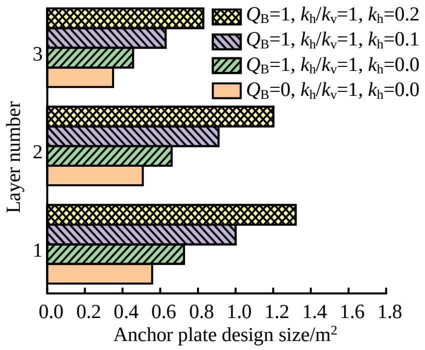

Fig. 21 Design sizes of anchor plates for each layer considering different seismic and rainfall intensities with linear distribution

Furthermore, the anchor plate body is buried in the backfill and should be situated in a stable area of the soil outside the potential critical slip surfaces. The anchor plate is connected to the beam-column nodes of the lattice frame through tie rods. The earth pressure acts on the concrete frame system, and the external force will be transferred to the anchor plate through the tie rod. The stability of the frame structure and the whole slope is maintained by the pull-out capacity provided by the anchor plate acting on the stabilized soil[6]. Figure 22 shows the horizontal lengths of the free sections for each layer of anchor plates under the most unfavorable conditions, which could facilitate the design of the tie rod lengths. During the design process, it is essential to ensure that the anchor plate body is situated in the stable zone of the soil.

To verify the correctness of the equations in this paper, the strength reduction method is used to analyze the stability of the slope. Since the active earth pressure is consistent with the pull-out capacity of the anchor plate at the limit equilibrium state, both the shear strength parameters c and ψ are reduced to achieve the limit equilibrium state of the slope. The corresponding reduction coefficient $F_{\rm s}$ is the calculated safety factor, as shown in the following equation:

$$
\begin{aligned}
&P_{\rm a}(r_0\cos\theta_0-D)=\\
&\int_{\theta_0}^{\theta_1} r^2\left(\frac{\psi}{F_{\rm s}}\sigma^{\rm s}-\frac{c'}{F_{\rm s}}\right){\rm d}\theta+\int_{\theta_0}^{\theta_1}[r^2\sin\theta\gamma(1\pm k_{\rm v})\cdot\\
&(r\cos\theta-r_1\cos\theta_1)(-\frac{\psi}{F_{\rm s}}\sin\theta+\cos\theta)]{\rm d}\theta+\\
&\int_{\theta_0}^{\theta_1}[k_{\rm h}\gamma(r\cos\theta-r_1\cos\theta_1)(\frac{r\cos\theta+r_1\cos\theta_1}{2})\cdot\\
&(r\cos\theta-r\frac{\psi}{F_{\rm s}}\sin\theta)]{\rm d}\theta-\\
&\frac{1}{2}\gamma(1\pm k_{\rm v})H^2\tan w(\frac{H}{3}\tan w+r_0\sin\theta_0)-\\
&\frac{1}{2}k_{\rm h}\gamma H^2\tan w(r_0\cos\theta_0-\frac{2}{3}H)+\\
&[Q(1\pm k_{\rm v})(r_1\sin\theta_1-r_0\sin\theta_0-H\tan w)\cdot\\
&\frac{1}{2}(r_0\sin\theta_0+H\tan w+r_1\sin\theta_1)+k_{\rm h}Q\cdot\\
&(r_1\sin\theta_1-r_0\sin\theta_0-H\tan w)(r_0\cos\theta_0-H)]-\\
&\sum_{i=1}^{n}T_{{\rm p}i}(r_0\cos\theta_0-D_i)
\end{aligned}
\tag{40}
$$

where $T_{{\rm p}i}$ is the ultimate pull-out capacity that the i-th layer of anchor plates can provide; D_i is the height of the i-th layer of anchor plates from the ground surface; and $\sum_{i=1}^{n}T_{{\rm p}i}$ is the sum of the ultimate pull-out capacity of all layers of anchor plates.

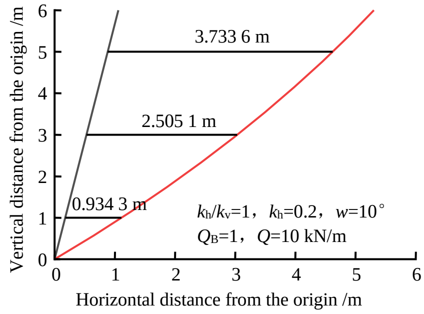

Fig. 22 Horizontal distances within slope slip surface trajectory under most unfavorable working condition

Through the above analysis and calculation, without considering the effects of rainfall and seismic activity ($Q_{\rm B}=0$, $k_{\rm h}=k_{\rm v}=0$), it is required to install 0.403 5, 0.706 1 and 0.608 8 m²of anchor plates per unit width of the slope to achieve a critical equilibrium state for the slope from bottom to top, as illustrated in Fig. 14. Equation (40) yields a slope safety factor of 1.005, indicating that the slope is close to its critical state. Furthermore, increasing the area of the anchor plates by 1.5 times, the corresponding safety factor will be raised to 1.279.

Under the most unfavorable conditions ($Q_{\rm B}=1$, $k_{\rm h}=k_{\rm v}=0.2$), it is required to install 0.915 0, 1.601 3 and 1.380 6 m²of anchor plates per unit width of the slope to achieve a critical equilibrium state for the slope from bottom to top, as illustrated in Fig. 20. Equation (40) yields a slope safety factor of 0.990 1, indicating that the slope is close to its critical state. Furthermore, increasing the area of the anchor plates by 1.5 times, the corresponding safety factor will be raised to 1.480 4, which satisfies the design requirements for slope stability.

5 Conclusions

(1) Based on the limit equilibrium method and the log-spiral slip surface, the calculation equation for the active earth pressure of unsaturated soil is obtained by considering transient seepage and seismic effects.

(2) By combining the equations for the active earth pressure of unsaturated soil and the pull-out capacity of anchor plate, the equation for calculating the design size of anchor plates is obtained. Furthermore, the minimum design length of the tie rod in the free section of the anchor plate is derived by analyzing the trajectory of the most critical slip surface.

(3) The influence of weak rainfall ($Q_B \leqslant 0.5$) on the design size of anchor plates can be neglected (with increment less than 2%). However, the effect of heavy rainfall and seismic effects on the design size of anchor plates is significant. When considering heavy rainfall ($Q_B = 1$) and seismic effects ($k_h / k_v = 1$, $k_h = 0.2$) separately, the increase in design size of anchor plates can reach 30.31% and 103.17%, respectively. When considering combined heavy rainfall and strong seismic effects, the increase can reach 136.71%.

(4) During the design of anchor plate size, the trapezoidal distribution leads to a safer design.

References

[1] ZHUANG P Z, YUE H Y, SONG X G, et al. Pullout behaviour of inclined shallow plate anchors in sand[J]. **Canadian Geotechnical Journal**, 2022, 59(2): 239−253.

[2] SHAHRIAR A R, ISLAM M S, JADID R. Ultimate pullout capacity of vertical anchors in frictional soils[J]. **International Journal of Geomechanics**, 2020, 20(2): 04019153.

[3] HANNA A, RAHMAN F, AYADAT T. Passive earth pressure on embedded vertical plate anchors in sand[J]. **Acta Geotechnica**, 2011, 6(1): 21−29.

[4] BHATTACHARYA P, KUMAR J. Pullout capacity of inclined plate anchors embedded in sand[J]. **Canadian Geotechnical Journal**, 2014, 51(11): 1365−1370.

[5] KAME G S, DEWAIKAR D M, CHOUDHURY D. Pullout capacity of a vertical plate anchor embedded in cohesion-less soil[J]. **Earth Science Research**, 2012, 1(1): 27−56.

[6] ZHU Yan-peng, TAO Jun, YANG Xiao-hui, et al. Design and numerical analysis of reinforced high fill slope with frame prestressed anchor plate structure[J]. **Rock and Soil Mechanics**, 2020, 41(2): 612−623.

[7] PENG J G, VAHEDIFARD F. Passive and active earth pressures in unsaturated soils under transient flow using a curved failure mechanism[J]. **International Journal of Geomechanics**, 2023, 23(7): 04023087.

[8] LI Yu-nong, LIU Chang, WANG Li-wei. Ultimate stability analysis of three-dimensional heterogeneous soil slopes under seismic effects[J]. **Rock and Soil Mechanics**, 2022, 43(6): 1493−1502.

[9] TANG Shi-xiong, DENG Guang-hui, LIU Heng-qiu. Research on the application of quasi-static method in slope seismic stability analysis[J]. **Urban Geology**, 2020, 15(2): 181−186.

[10] ZHANG Chang-guang, GUAN Gang-hui, LI Hai-xiang, et al. Seismic active earth pressure on a retaining wall in unsaturated soils with cracks for changing water table[J]. **Rock and Soil Mechanics**, 2023, 44(6): 1575−1584.

[11] MING Y, MURFF J D, AUBENY C P. Undrained capacity of plate anchors under general loading[J]. **Journal of Geotechnical and Geoenvironmental Engineering**, 2010, 136(10): 1383−1393.

[12] SHAHROKHABADI S, VAHEDIFARD F, GHAZANFARI E, et al. Earth pressure profiles in unsaturated soils under transient flow[J]. **Engineering Geology**, 2019, 260(C): 105218.

[13] HAN Jia-ming, DONG Zhao, SU San-qing, et, al. Analytical solution of rainfall infiltration in homogeneous unsaturated slope and its application in loess slope[J]. **Rock and Soil Mechanics**, 2023, 44(1): 241−250.

[14] ZHU F. Geosynthetic reinforced earth structures: effects of facing units and force distribution functions[D]. Newark: University of Delaware，2008.

[15] LU N, LIKOS W J. Unsaturated soil mechanics[M]. New York: Wiley, 2004.

[16] LU N, LIKOS W J. Suction stress characteristic curve for unsaturated soil[J]. **Journal of Geotechnical and Geoenvironmental Engineering**, 2006, 132(2): 131−142.

[17] GODT J W, SENER-KAYA B, LU N, et al. Stability of infinite slopes under transient partially saturated seepage conditions[J]. **Water Resources Research**, 2012, 48(5): W05505.

[18] SRIVASTAVA R, YEH T C J. Analytical solutions for one-dimensional, transient infiltration toward the water table in homogeneous and layered soils[J]. **Water Resources Research**, 1991, 27(5): 753−762.

[19] BAKER R, GARBER M. Theoretical analysis of the stability of slopes[J]. **Geotechnique**, 1978, 28(4): 395−411.

[20] LESHCHINSKY D, FAN Z. Resultant force of lateral earth pressure in unstable slopes[J]. **Journal of Geotechnical and Geoenvironmental Engineering**, 2010, 136(12): 1655−1663.

[21] VAHEDIFARD F, LESHCHINSKY D, MEEHAN C L. Relationship between the seismic coefficient and the unfactored force of geosynthetic in reinforced earth structures[J]. **Journal of Geotechnical and Geoenvironmental Engineering**, 2012, 138(10): 1209−1221.

ALLEN T M, BATHURST R J. Prediction of reinforcement loads in reinforced soil walls[R]. Olympia, Washington: Washington State Department of Transportation, 2003.